This is a preprint, the final version is subject to change, of the American Mineralogist (MSA)
Cite as Authors (Year) Title. American Mineralogist, in press.
(DOI will not work until issue is live.) DOI: http://dx.doi.org/10.2138/am-2017-5982

#Revision 2:

Dolomite dissociation indicates ultra-deep (>150 km) subduction of a garnet-bearing dunite block (the Sulu UHP terrane)

Bin Su [1, 3], Yi Chen [1, 2]*, Shun Guo[1, 2], Jing-Bo Liu[1]

[1]State Key Laboratory of Lithospheric Evolution, Institute of Geology and Geophysics, Chinese Academy of Sciences, P.O. Box 9825, Beijing 100029, China

[2]CAS Center for Excellence in Tibetan Plateau Earth Sciences, Beijing 100101, China

[3]University of Chinese Academy of Sciences, Beijing 100049, China

* Corresponding author. Tel: +86 010 82998534; fax: +86 010 62010846.

E-mail address: chenyi@mail.iggcas.ac.cn (Y. Chen), subin@mail.iggcas.ac.cn (B. Su)

Running Title: Ultra-deep subduction of the Sulu dunite block

ABSTRACT

The dissociation of dolomite into magnesite and aragonite has been regarded as a useful indicator for ultrahigh-pressure (UHP) metamorphism. In this study we investigate an unusual texture involving magnesite and calcite intergrowths with dolomite relicts in a garnet-bearing dunite block from the Sulu UHP terrane, eastern China. The carbonate intergrowths typically occur as interstitial grains with low dihedral angles against surrounding olivines and have a dolomitic precursor composition. Our observations indicate that the carbonate intergrowths were initially inherited from the well-documented magnesite and aragonite assemblage after dolomite dissociation. The initial dolomite grains were likely to crystallize during the dolomitic melt metasomatism within the shallow lithospheric mantle. A series of experimental studies have well determined the equilibrium boundary of dolomite = magnesite + aragonite greater than 5 GPa along a wide temperature range, which provides direct evidence that the dunite block has ever subducted to depths greater than 150 km during the Triassic continental subduction. The preservation of magnesite and aragonite (now calcite) intergrowths without dolomite synthesis reaction during exhumation is probably due to the lack of fluid and rapid decompression from the peak stage to the calcite stability field. In this study, we suggest that dunite blocks from high-pressure and UHP terranes could have subducted to UHP conditions similar to garnet lherzolite and pyroxenite and were then entrained into slab slices rapidly en route to the surface.

Keywords: dunite, dolomite dissociation, ultra-deep subduction, Sulu belt

INTRODUCTION

Orogenic peridotite bodies of various sizes are minor but significant components within high-pressure (HP) and ultrahigh-pressure (UHP) terranes in orogenic belts. They originated mainly from the mantle wedge above subducting crust and later were tectonically emplaced into subduction channel to various depths (50–200 km) before exhumation (Brueckner and Medaris 2000; Zhang et al. 2000; Scambelluri et al. 2008). Therefore, orogenic peridotites act as a natural laboratory to disclose the mass transfer from the downgoing slab into the overlying mantle wedge (Scambelluri et al. 2006; Malaspina et al. 2009; Chen et al. 2017), as well as the geodynamics of ultra-deep subduction (van Roermund et al. 2002; Ye et al. 2009). Compared with garnet lherzolites, which record important aspects of crust–mantle interactions and multistage metamorphic events in subduction zones (Zanetti et al. 1999; Sapienza et al. 2009), orogenic dunites lack the petrological and mineralogical imprints of these processes (Beyer et al. 2006; Chen et al. 2009). In this regard, orogenic dunites, despite their wide distribution in HP and UHP terranes, have not attracted enough attention in previous investigations of orogenic peridotites.

However, orogenic dunites, with their upper mantle nature largely intact, are the best lithology among orogenic peridotites for tracing the provenances and initial compositions and can also shed light on the mantle wedge evolution prior to the onset of subduction (Kubo 2002; Beyer et al. 2004; Chen et al. 2015; Su et al. 2016a). They commonly exhibit different chemical and physical properties (e.g., density, wave velocity, viscosity and magnetic conductivity) from garnet lherzolites

(e.g., Lee 2003; Griffin et al. 2009). Understanding the distribution ranges (or depths) of these dunites in subduction zones may thus expand our knowledge of geochemical/geophysical heterogeneity in the mantle wedge. In general, orogenic dunites occur as minor components within larger bodies of lherzolite and harzburgite (Beyer et al. 2006; Zhang et al. 2008; Song et al. 2009), but there are also several blocks dominated by dunite, such as Otrøy in the Western Gneiss Region (Spengler et al. 2006) and Ganyu and Lijiatun in the Sulu region (Chen et al. 2009; Su et al. 2016a). These dunite blocks mostly represent fragments of subcontinental lithospheric mantle (SCLM) characterized by highly depleted compositions (see review in Su et al. 2016b).

Although orogenic dunites have a great advantage over garnet lherzolites in addressing the early histories of orogenic peridotites, their geodynamic processes related to the slab subduction and exhumation are still poorly defined due to their simple mineral assemblages. Given the wide occurrence of spinel and lack of garnet in orogenic dunites, previous work suggested that dunite blocks have not undergone UHP metamorphism, but were derived from fore-arc depths ($P < 2$ GPa) (e.g., Zheng et al. 2008; Xie et al. 2013; Li et al. 2016). However, the stability field of spinel can extend to much higher pressures in Al-poor ultramafic rocks (Klemme 2004; Ziberna et al. 2013). This raises an important question of how to evaluate whether dunite blocks have subducted to UHP conditions. Identification of UHP indicators for orogenic dunites will give further important constraints on the processes of continental subduction channel.

In this paper we present a study of a garnet-bearing dunite block near the village of Lijiatun in the northern Sulu UHP terrane of eastern China (Fig. 1). Its origin and metasomatic histories have been assessed in our recent work (Su et al. 2016a). Here, we focus on the magnesite–calcite–dolomite intergrowth resulting from dolomite dissociation to reveal the ultra-deep subduction and exhumation processes of the dunite block. Our new data suggest that the Lijiatun dunite block had ever subducted to depths greater than 150 km and then probably experienced a rapid ascent to shallow depths (<60 km). Mineral abbreviations used in the text, figures and tables all follow Whitney and Evans (2010).

GEOLOGICAL BACKGROUND

The Sulu UHP terrane is located in the eastern part of the Dabie–Sulu orogenic belt created by the subduction of the Yangtze block below the North China craton during the Triassic (Li et al. 1993; Zhang et al. 2009). The occurrences of coesite, diamond and mineral exsolution microstructures in the crustal metamorphic rocks indicate that the Yangtze block had been subducted to exceptional depths of 200 km and then exhumed to the surface (Xu et al. 1992; Ye et al. 2000a, b; Liu et al. 2001). In addition to bodies of eclogite, marble and quartzite within the country UHP gneisses, peridotite blocks consisting mainly of garnet lherzolite with minor harzburgite, dunite and pyroxenite occur sporadically throughout the Sulu terrane. These peridotites are generally divided into two groups: mantle-derived peridotites (Type A) and crust-hosted peridotites (Type B) [see Zhang et al. (2000) for further

106 details]. Except for dunite (e.g., Lijiatun), most Sulu garnet peridotites are
107 recognized to have undergone *in situ* subduction-zone UHP metamorphism with
108 peak pressures of 3.5–7.0 GPa (e.g., Yang and Jahn 2000; Zhang et al. 2008; Ye et al.
109 2009) and to have simultaneously experienced multiple metasomatic events
110 associated with slab-derived liquids at various depths (Malaspina et al. 2009; Chen
111 et al. 2013b). In contrast, the metamorphic histories of dunites related to the
112 continental subduction are still poorly constrained to date.

113 The Lijiatun block (~200×400 m^2 in size) is surrounded by gneisses and is
114 exposed in the northern Sulu terrane (Fig. 1). It is dominated by dunite in the interior
115 and serpentinite (after dunite) at the margin (Fig. 2a). A recent study by Su et al.
116 (2016a) suggests that the Lijiatun dunites originated from the SCLM beneath the
117 North China craton (NCC). They were the residues after high degrees of partial
118 melting in the early Proterozoic, and then underwent dolomitic melt metasomatism
119 in the shallow lithospheric mantle prior to their incorporation into the subduction
120 channel. During the Triassic continental subduction, they experienced weak
121 metasomatism by slab-derived fluids at shallow mantle depths (Su et al. 2016a).
122 However, the subduction depth and geodynamic processes during the continental
123 subduction are still enigmatic. Although Ren et al. (2007) calculated a peak pressure
124 of 3.0–4.1 GPa using the Grt–Opx geobarometer (Brey and Köhler 1990), the peak
125 mineral compositions were modified during exhumation, as discussed in the
126 following section.

127

PETROGRAPHY

The petrography of the Lijiatun dunites has been presented in detail by Su et al. (2016a). The dunite samples mainly consist of olivine (~65 vol.%) and serpentine (~24 vol.%), with minor orthopyroxene (~8 vol.%), Cr-spinel/chromite (~1 vol.%), amphibole (~2 vol.%), clinopyroxene, garnet, carbonate phases, chlorite and talc. Serpentine commonly cuts the matrix olivine into several fragments (Fig. 2), indicating that serpentine was mostly derived from olivine metasomatized by silica-rich aqueous fluids in the late stage. Some secondary olivine and clinopyroxene occur as olivine-rich veins crosscutting orthopyroxene (Fig. S1 in the supplemental materials), following the reaction orthopyroxene + dolomite (melt) = olivine + clinopyroxene + CO_2 (Su et al. 2016a). This study focuses on the carbonate phases.

The carbonate phases are divided into two types: calcite veinlets and isolated grains. The former cut through original minerals and can extend along an entire thin section (Fig. 2b); hence, they formed during the final stage and are thus ignored in the following section. The latter are anhedral and interstitial grains (0.1–0.5 mm in diameter) among matrix olivines (or serpentine after olivine) and are far from pyroxenes and secondary hydrous minerals (Fig. 2c). The boundaries of the carbonate grains are well defined, and they typically have low dihedral angles against the surrounding olivines (Figs. 2d–2f), pointing to inheritance from an initial melt-filled pore. In Figs. 2g–2i, these carbonate grains comprise an intimate intergrowth of magnesite and calcite (Raman spectra at 1086, 714, 281 and 156 cm^{-1}),

150 which show a symplectite-like texture (Figs. 3a and 3b). The volumetric proportions
151 of magnesite and calcite are estimated to be 40–43% and 57–60%, respectively,
152 based on backscatter electron (BSE) images using Adobe® Photoshop and the
153 ImageJ software (W. S. Rasband, http://rsb.info.nih.gov/ij/). In the high-resolution
154 transmission electron microscope (TEM) image, a prominent boundary is present
155 between magnesite and calcite, and no other phases (e.g., dolomite) occur at the
156 interface (Fig. 4). Small dolomite grains (<3 μm) are locally preserved as relicts in
157 calcite (Figs. 3c–3f).

158 Trace interstitial garnets with small grain sizes (10–80 μm in diameter) occur as
159 round grains in the matrix (Figs. 5a–5c), but several irregular and elongated grains
160 are also present (Fig. 5d). A few circular olivines are included in garnet. All garnets
161 are fresh without any retrograde rims. No pyroxene or spinel is in direct contact with
162 these garnets.

163 Hydrous minerals (amphibole, chlorite and talc) occur in the matrix, with minor
164 chlorite and serpentine found as inclusions in spinel. Amphibole grains after
165 pyroxene or in the matrix with minor orthopyroxene relict inclusions generally
166 appear as anhedral grains (Figs. 5e and 5f), and a few amphibole-rich veins with
167 millimeter to centimeter widths are observed in hand specimens (Fig. 5g). Trace
168 chlorite and talc occur in association with amphibole (Figs. 5e and 5f), and no
169 replacement relationships are present between these hydrous minerals, indicating
170 that they formed during the same stage.

171

ANALYTICAL METHODS

High-resolution BSE imaging and semi-quantitative energy dispersive spectroscopy (EDS) analyses of carbonate and silicate minerals were conducted using a field emission scanning electron microscope (FEI Nova NanoSEM 450) at the Institute of Geology and Geophysics, Chinese Academy of Sciences (IGGCAS). The measurement was performed at a 10 kV acceleration voltage and a 0.5 nA current, with a working distance of approximately 6 mm. The polymorphs of $CaCO_3$ were examined by micro-Raman spectroscopy using a HORIBA Jobin–Yvon LabRAM HR 800 at the IGGCAS.

A thin slice with an area of 7.5 μm × 4.5 μm was cut across the interface between magnesite and calcite and polished to ~100 nm in thickness using a focused ion beam (FIB) system on a Zeiss Auriga Compact instrument at the IGGCAS. A JEOL JEM-2100HR TEM was used to investigate the FIB-cut carbonate section. The TEM instrument was operated with an accelerating voltage of 200 kV and a beam current of 100 μA for standard bright-field TEM observations and energy-dispersive X-ray spectrometry analyses.

Major element compositions of minerals were determined using a Cameca SXFive electron probe microanalyzer (EPMA) at the IGGCAS. The analytical conditions were a 15 kV accelerating voltage and a 10 nA beam current with a focused beam for carbonate minerals and 15 kV, 20 nA and a defocused beam of 1 μm in diameter for silicate minerals. In addition, broad beam analyses using a defocused beam of 20 μm in diameter were performed to obtain the integrated

194 composition of the carbonate intergrowth. The counting times were 20 s on peak and
195 10 s on each background position. Natural and synthetic silicates (+oxides) and
196 carbonates were used as standards for silicate and carbonate analyses, and the
197 analytical uncertainties for most major elements were less than 1.5%. The Fe^{3+}
198 abundance in garnet was determined by charge balance (Droop 1987). The
199 end-members of garnet discussed in this study include: almandine (Alm), pyrope
200 (Prp), grossular (Grs), andradite (Adr) and knorringite (Knor). The formulas used to
201 calculate the proportions of these end-members in garnet are given in the footnote of
202 Table 2.
203
204 **MINERAL CHEMISTRY**
205 Detailed major element compositions of several minerals (olivine,
206 orthopyroxene, spinel, clinopyroxene and amphibole) are shown in Su et al. (2016a)
207 and are briefly summarized as follows: **olivine** Mg# values [atomic $Mg/(Mg+Fe^{2+})$
208 $\times 100$] range from 92.0 to 92.6; **orthopyroxene** porphyroblast (Opx-P) cores before
209 exsolution have high CaO (1.08–1.49 wt%) and Al_2O_3 (1.70–1.93 wt%) contents,
210 and the recrystallized rims have low CaO (0.06–0.14 wt%) and Al_2O_3 (0.32–1.16
211 wt%) contents; **clinopyroxene** is close to the diopside end-member, with high Mg#
212 values (95.9–96.7); **spinel** is chromium-rich, with Cr/(Cr+Al) (atomic ratio) values
213 from 0.50 to 0.73 and Mg# from 38.5 to 55.1; **amphibole** after orthopyroxene is
214 pargasitic with a high Tschermak component and low K_2O content (<0.62 wt%),
215 whereas minor amphibole after clinopyroxene has a tremolitic component.

Representative mineral compositions are given in Table 1 and 2. **Magnesite** from the symplectite-like intergrowth is relatively magnesian at $Mgs_{89.0–91.5}Sd_{8.0–10.4}Cal_{0–0.2}$. **Calcite** ranges from nearly pure $CaCO_3$ to $Cal_{97.4}$ $Mgs_{2.3}Sd_{0.3}$. Because neither Mg nor Fe was detected in calcite using TEM-EDS (Fig. 4d), the few Mg and Fe contents in calcite may be due to beam overlap with surrounding magnesite during electron probe analyses. A series of TEM-EDS analyses show that diffusion of Ca in magnesite and Mg in calcite across the interface is very limited (<20 nm) (Figs. 4d–4h), in consistent with previous studies (e.g., Fisler and Cygan 1999). The composition of **dolomite** relicts in calcite cannot be directly measured owing to their small grain sizes. The EDS analyses show that the dolomite contains an extremely low siderite component (Fig. S2 in supplemental materials). The precursor composition of the carbonate intergrowth, roughly measured by EPMA with a broad beam (20 μm), shows a dolomite component ($Cal_{49}Mgs_{47}Sd_4$), which was also obtained by broad-beam EDS analyses (Fig. S2 in the supplemental materials) and reintegration of the disaggregated products (Figs. 3a and 3b). As 1 mole of calcite occupies 32% more volume than 1 mole of magnesite (Holland and Powell 2011), mole ratios of Ca/Mg from the intergrowth are approximately equal to one (1.01–1.12), based on the volumetric proportions of calcite and magnesite. All these carbonate phases contain extremely low BaO, SrO, Na_2O and K_2O contents.

Garnet exhibits a small compositional variation, with 4.14–5.65 wt% CaO, 0.74–1.46 wt% Cr_2O_3 and Mg# values of 78.3–79.8, similar to the values in garnet lherzolite from the Sulu terrane (Zhang et al. 2008; Ye et al. 2009). In general, the

238 inner portions are homogeneous, with a relatively high grossular component (10.0–
239 13.0 mol%) and a low andradite component (<2.0 mol%). Towards the rims, the
240 grossular and andradite components decrease (down to 6.1 mol%) and increase,
241 respectively. In some garnet grains, the grossular component displays a symmetrical
242 zoning pattern that smoothly decreases from core to rim, whereas knorringite,
243 almandine and pyrope do not show significant changes (Fig. 6).
244

245 **DISCUSSION**

246 **Dissociation reaction of dolomite = magnesite + aragonite**

247 The observed magnesite and calcite intergrowths show low dihedral angles and
248 occur as interstitial grains among matrix olivines (Figs. 2c–2f), indicating that they
249 were initially derived from an infiltrating carbonate melt (Ionov et al. 1993; Kogarko
250 et al. 2001). The precursor composition of the carbonate melt has a dolomite
251 stoichiometry, as measured by several methods (Table 1 and Fig. S2). Three possible
252 stages for this melt infiltration are proposed to account for the carbonate
253 intergrowths.

254 First, dolomitic melt might be incorporated into the dunite during exhumation.
255 Experimental studies have demonstrated that pressure has a significant effect on the
256 crystallized product in the $CaCO_3$–$MgCO_3$ melt system (Irving and Wyllite 1975;
257 Byrnes and Wyllite 1981; Buob et al. 2006). At pressures <~5 GPa, the final
258 products, in turn, are Arg/Cal, Arg/Cal+Dol, Dol, Dol+Mgs and Mgs from the Ca
259 side to Mg side at subsolidus temperatures. The intergrowth of Mgs+Cal/Arg cannot

be observed in the products generated at pressures less than ~5 GPa (e.g., Irving and Wyllite 1975; Byrnes and Wyllite 1981; Buob et al. 2006), indicating that this assumption is impossible.

Second, if dolomitic melt infiltration occurred during subduction to pressures >~5 GPa, a dolomite solid solution phase (Dol_{ss}) would first crystallize from carbonate melts with a wide Ca/Mg range during cooling (~1400 °C) and finally break down into a Mgs+Arg intergrowth at 800–1000 °C (Buob et al. 2006). Experimental studies suggest that the magnesite and calcite (or aragonite) intergrowth was unlikely to directly quench from a dolomitic melt along a wide pressure range but could form from solid dolomite dissociation under UHP conditions (>5 GPa) (Shirasaka et al. 2002; Buob et al. 2006). However, the solidi of carbonated eclogite, carbonated pelite and marble (~1000–1400 °C), which are the potential sources for carbonate melts in subduction zones (Irving and Wyllite 1975; Hammouda 2003; Dasgupta et al. 2004; Buob et al. 2006; Grassi and Schmidt 2011), are much hotter than the typical peak temperatures of exhumed UHP rocks (e.g., Zhang et al. 2009; Proyer et al. 2013; Guo et al. 2015). Therefore, it is unlikely that dolomitic melts were derived from subducted crust at depths <200 km. Furthermore, carbonate melts from subducted crust are typically rich in Ca and Fe with a low Mg# values (Hammouda 2003; Dasgupta et al. 2004; Thomsen and Schmidt 2008). Such compositions are markedly different from that of the carbonate intergrowths in this study (Fe-poor dolomite without any alkalis), which further rules out the possibility of dolomitic melt infiltration in subduction zones.

Third, the dolomitic melt infiltration is more likely to have occurred prior to subduction. Our former paper indicates that the Lijiatun dunites underwent dolomitic melt metasomatism within the shallow lithospheric mantle (Su et al. 2016a). This metasomatism is characterized by the formation of olivine + clinopyroxene veins crosscutting orthopyroxene porphyroblasts (Opx+Dol=Ol+Cpx+CO_2), as shown in the supplemental materials (Fig. S1). During the metasomatic reaction, dolomitic melt reacted out in Opx-rich domains, but dolomite could crystallize during this melt infiltration in Opx-absent domains. This relationship is supported by the observed textures: the dolomite (carbonate intergrowth) only occurs in olivine domains and is not in contact with orthopyroxene (Figs. 2c–2f). The occurrence of carbonate minerals after carbonate metasomatism has widely been reported in mantle peridotites (e.g., Ionov et al. 1993; Kogarko et al. 2001; Morishita et al. 2003; Naemura et al. 2009).

Therefore, the magnesite and calcite (or aragonite) intergrowths cannot directly quench from a dolomitic melt and is better explained by solid dolomite dissociation. This finding is further supported by occurrence of dolomite relicts in the intergrowths (Figs. 3c–3f). Experimental studies indicate that the initial products of dolomite dissociation are magnesite and aragonite (Martinez et al. 1996; Luth 2001). Although no aragonite relic can be found in calcite, the fact that magnesite cannot coexist with calcite anywhere in *P*–*T* space (e.g., Proyer et al. 2013) implies that at least one of them has been replaced by a secondary phase. As the intergrowths can be only observed interstitially along olivine boundaries, the “pressure vessel” is not

304 present for these interstitial aragonites. A similar process has been observed for the
305 fast transition of interstitial coesite to quartz (Schertl et al. 1991; O'Brien and
306 Ziemann 2008). Phase transition from aragonite to calcite is even faster than that of
307 coesite-to-quartz (Carlson and Rosenfeld 1981; Korsakov et al. 2009; Lü et al. 2014),
308 indicating that interstitial aragonite would be immediately replaced by calcite under
309 low-pressure conditions. The magnesite may be well preserved because
310 clinopyroxene is so rare in the matrix that the reaction of magnesite + clinopyroxene
311 = dolomite + orthopyroxene would not occur during exhumation. Therefore, the
312 most likely process was that the observed magnesite and calcite intergrowth was
313 inherited from magnesite + aragonite symplectite, which originally formed from
314 dolomite dissociation. The symplectitic intergrowth texture of magnesite + aragonite
315 is common in dolomite dissociation experiments (e.g., Shirasaka et al. 2002; Buob et
316 al. 2006).
317
318 **Ultra-deep (>150 km) subduction**
319 The *P*–*T* conditions of dolomite dissociation reaction have been determined by
320 many experimental studies with different starting materials, experimental methods
321 and/or run durations (Martinez et al. 1996; Luth 2001; Sato and Katsura 2001;
322 Shirasaka et al. 2002; Buob et al. 2006; Hermann et al. 2016). All studies
323 consistently indicate that dolomite breakdown occurs at pressures higher than 5 GPa
324 between 500 and 1200 °C (Fig. 7). Therefore, the equilibrium magnesite + aragonite
325 assemblage after dolomite can be regarded as the third index reaction for UHP

metamorphism after the quartz/coesite and graphite/diamond transitions (e.g., Sato and Katsura 2001; Zhang et al. 2003). In recent decades, coexisting dolomite, magnesite and aragonite (or pseudomorphs after them) have been identified in marbles, eclogites and metapelites from several UHP terranes (Zhang and Liou 1996; Zhang et al. 2003; Dobrzhinetskaya et al. 2006; Proyer et al. 2013) but rarely in orogenic peridotites.

As shown in Fig. 7, after extensive melt extraction, the Lijiatun dunites experienced dolomitic melt metasomatism within the shallow lithospheric mantle, which resulted in partial orthopyroxene dissolution and secondary olivine and clinopyroxene precipitation (Su et al. 2016a). Meanwhile, some dolomites interstitially crystallized from the dolomitic melt in Opx-absent domains (Figs. 2c–2f). During the Triassic continental subduction, the dunites were incorporated into the subduction channel, and dolomite potentially acted as a pressure indicator. Given that the interstitial dolomite only occurs in olivine domains and is far from orthopyroxene in the Lijiatun dunites, the reaction of dolomite + orthopyroxene = magnesite + clinopyroxene would not take place during dunite subduction and dolomite could be stable until its dissociation. Likewise, orthopyroxene would not be exhausted on such a reaction with increasing pressure. As stated in the above section, the magnesite and calcite intergrowths represent the products of dolomite dissociation, pointing to the UHP (>5 GPa) metamorphism of the Lijiatun dunites (Fig. 7). Therefore, the carbonate intergrowth indicates that the dunite block have ever subducted to depths greater than 150 km, similar to the widespread garnet

lherzolites from the Dabie–Sulu terrane (Yang and Jahn 2000; Zhang et al. 2008; Ye et al. 2009). It is worth noting that the reaction curve shifts toward lower pressure with the addition of Fe to the dolomite (Franzolin et al. 2012), but this addition has little effect on the results of this study due to the high Mg# values (> 90).

In previous investigations, conventional thermobarometers, including Grt–Opx geobarometers (Harley 1984; Nickel and Green 1985; Brey and Köhler 1990) and Grt–Cpx geothermometers (Ai 1994; Ravna 2000), have been widely used to yield the *P*–*T* conditions of peridotites. With respect to the Lijiatun dunites, as they experienced high-degree (~30%) melting at low pressure (<4 GPa; Su et al. 2016a), initial garnets (if present) were inevitably exhausted (Walter 1998). The tiny interstitial garnets were thus formed during the deep subduction (Figs. 5a–5d). Their growths could be approached by the continuous reaction Mg (Al, Cr)$_2$O$_4$ (Spl) + 2Mg$_2$Si$_2$O$_6$ (Opx) = Mg$_3$(Al, Cr)$_2$Si$_3$O$_{12}$ (Grt) + Mg$_2$SiO$_4$ (Ol) (Brey et al. 1999; Girnis et al. 2003; Klemme 2004), and the chemical zoning in garnet corresponds to a prograde growth process (Fig. 6). Therefore, it is possible to constrain the peak *P*–*T* conditions from the compositions of garnet rim and pyroxene using the above thermobarometers. However, the peak compositions of pyroxenes have been modified during the exhumation stage, which makes the results inferred from conventional thermobarometers less reliable. Specifically, as the low-Al$_2$O$_3$ Opx-P rims have been resorbed by amphibole to different extents during the late fluid metasomatism stage (Fig. 2f in Su et al. 2016a), their compositions would have re-equilibrated at relatively lower pressures and, hence, the calculated peak pressures

(2.7–4.3 GPa) using the Grt–Opx geobarometer are underestimated. Due to the small size of clinopyroxene and its very minor presence in terms of modal composition, Mg–Fe exchange between clinopyroxene and surrounding minerals during cooling would easily reset its composition. Thus, the calculated temperatures (520–620 °C) by the Grt–Cpx thermometers are invalid for the peak conditions. In contrast, the garnet was free from retrograde modification (Figs. 5a–5d) and the approximately constant Mg# values in garnet from core to rim (Table. 2) can yield a nearly isothermal compressional *P–T* path for the Lijiatun dunite (thermodynamic modeling result, not shown) (Fig. 7). Similar prograde *P–T* paths have been reported in many mantle wedge-derived orogenic peridotites (e.g., Scambelluri et al. 2008; Ye et al. 2009; Chen et al. 2013a).

Potential mechanism for the preservation of carbonate intergrowth

It is widely accepted that peridotite bodies can be passively transported from mantle depths to the surface by deeply subducted crust during buoyancy-driven exhumation (Brueckner 1998; Zhang et al. 2000; Scambelluri et al. 2006; Chen et al. 2013a). During exhumation, magnesite and aragonite are expected to back-react to dolomite, leaving only isolated magnesite and aragonite in coarse-grained dolomite, as reported in the Tianshan metapelites (Zhang et al. 2003) and the Dabie marbles (Proyer et al. 2013). However, the TEM results indicate that the dolomitization reaction did not occur at the interface between magnesite and calcite (after aragonite) in the Lijiatun dunites (Fig. 4), which was possibly due to low temperatures, a lack

392 of fluid flow, and/or rapid decompression. Experimental studies suggest that the
393 nucleation of a low-P dolomite from a high-P magnesite + aragonite assemblage may
394 be hindered by a kinetic barrier at low temperatures (Martinez et al. 1996; Sato and
395 Katsure 2001; Shirasaka et al. 2002), similar to the stishovite-to-coesite transition
396 (Zhang et al. 1996). The fact that the metamorphic temperatures of the Lijiatun
397 dunites (~800 °C) are higher than those of the Tianshan metapelites (~600 °C; Zhang
398 et al. 2003) and the Dabie impure marbles (600–800 °C; Proyer et al. 2013) argues
399 that sluggish reaction kinetics related to low temperature is not the major reason in
400 this study. In general, fluids play an important role in triggering and promoting
401 metamorphic reactions (Austrheim 1987; John and Schenk 2003). Unlike the above
402 metapelites and marbles exhibiting dolomite-forming reactions, the Lijiatun dunites
403 lacked fluids until their decompression to the calcite stability field, as minor hydrous
404 mineral assemblage (amphibole with trace chlorite and talc) after pyroxene mainly
405 formed at conditions of ~600–700 °C and <2 GPa (Naemura et al. 2009; Chen et al.
406 2013a; Scambelluri et al. 2014). The lack of fluid in the aragonite stability field
407 might have inhibited dolomite synthesis in this study, which has been used to explain
408 the preservation of metastable assemblages in UHP rocks (Liou and Zhang 1996;
409 Leech 2001). Moreover, the experiment of Shirasaka et al. (2002) shows that the
410 dolomite synthesis reaction occurs at pressures much lower than those of the
411 dissociation reaction, implying that the former is more sluggish than the latter. Thus,
412 a rapid decompression process might provide another a chance to preserve the
413 carbonate intergrowth during exhumation. Numerical modeling shows that mantle

414 wedge peridotite entrained in the subduction channel could be dragged to the surface
415 over a very short time (Gerya et al. 2002), and several peridotite blocks have been
416 shown to have experienced rapid exhumation after deep subduction (Gebauer 1996;
417 Olker et al. 2003; Hermann et al. 2006). A recent study by Yamato and Brun (2017)
418 suggests a catastrophic pressure drop for UHP rocks during the switch from burial to
419 exhumation in subduction zones. In the same way, if the Lijiatun dunites suffered
420 rapid decompression from the peak stage to the calcite stability field, aragonite
421 would have transformed to calcite immediately (Carlson and Rosenfeld 1981;
422 Korsakov et al. 2009). Because calcite could not react with magnesite to form
423 dolomite, the intergrowth of magnesite and calcite could be well preserved. In
424 summary, the preservation of magnesite and calcite intergrowth during the dunite
425 exhumation is potentially caused by a fluid-absent, rapid decompression process.
426

427 **IMPLICATIONS**

428 The discovery of microdiamond and majoritic garnet in orogenic peridotites
429 provides robust evidence that the peridotites were exhumed from depths of greater
430 than ~120 km and ~200 km, respectively (e.g., van Roermund and Drury 1998;
431 Brueckner et al. 2002; van Roermund et al. 2002; Song et al. 2004; Spengler et al.
432 2006). The deep origin of these rocks provides us a rare opportunity to explore the
433 processes active at great depths in subduction zones (Dobrzhinetskaya et al. 1996;
434 Scambelluri et al. 2008). In addition to the above two UHP index minerals, this study
435 shows that the dolomite dissociation reaction (Dol=Mgs+Arg) can also be used as a

436 reliable UHP indicator (>5 GPa) for orogenic peridotites. In this study, the
437 well-preserved magnesite–calcite–dolomite intergrowth represents the final products
438 of dolomite dissociation, suggesting that the dunite block had subducted to depths
439 greater than 150 km before exhumation, similar to the widely distributed garnet
440 lherzolites in the same terrane.

441 Dolomite together with magnesite is frequently reported in orogenic peridotites
442 (e.g., Zanetti et al. 1999; Zhang et al. 2007; Sapienza et al. 2009). Based on previous
443 studies and this work, the fate and stability of these minerals in orogenic peridotites
444 depend strongly on the bulk composition and peak pressures of the host peridotites
445 (e.g., Kushiro 1975; Wyllie et al. 1983). In fertile peridotites with abundant
446 orthopyroxene (e.g., garnet lherzolite), dolomite can be stable to depths of
447 approximately 100 km until it reacts out via the prograde reaction Opx + Dol = Cpx
448 + Mgs (Fig. 7; Kushiro 1975; Scambelluri et al. 2008). If orthopyroxene is absent or
449 rare (such as the Lijiatun dunite), dolomite can be stable up to much greater depths
450 (>5 GPa) until it breaks down into magnesite + aragonite. Thus, carbonate minerals
451 in dunites should be given more attention in the future study of orogenic peridotites.

452

453 **ACKNOWLEDGMENTS**

454 We thank Saihong Yang for help with the SEM analyses, Di Zhang and Qian
455 Mao for help with the EPMA analyses, Yijie Gao for help with the Raman analyses,
456 and Lixin Gu and Xu Tang for help with the TEM analyses. BS is grateful to
457 Xiaochun Li (The University of Hong Kong) for his helpful discussion. Critical

458 reviews by Jörg Hermann and an anonymous reviewer helped to improve the
459 manuscript. We also thank Jennifer Kung for handling this manuscript. This work
460 was funded by the National Basic Research Program of China (973 Program
461 2015CB856103), the National Science Foundation of China (Nos. 41372078,
462 41372080) and the National Postdoctoral Program for Innovative Talents
463 (BX201700239).

464

465 **REFERENCES CITED**

466 Ai, Y. (1994) A revision of the garnet–clinopyroxene Fe^{2+}–Mg exchange
467 geothermometer. Contributions to Mineralogy and Petrology, 115, 467–473.
468 Austrheim, H. (1987) Eclogitization of lower crustal granulites by fluid migration
469 through shear zones. Earth and Planetary Science Letters, 81, 221–232.
470 Beyer, E.E., Brueckner, H.K., Griffin, W.L., O'Reilly, S.Y., and Graham, S. (2004)
471 Archean mantle fragments in Proterozoic crust, Western Gneiss Region,
472 Norway. Geology, 32, 609–612.
473 Beyer, E.E., Griffin, W.L., and O'Reilly, S.Y. (2006) Transformation of Archaean
474 lithospheric mantle by refertilization: evidence from exposed peridotites in
475 the Western Gneiss Region, Norway. Journal of Petrology, 47, 1611–1636.
476 Brey, G.P., and Köhler, T. (1990) Geothermobarometry in four-phase lherzolites II.
477 New thermobarometers, and practical assessment of existing
478 thermobarometers. Journal of Petrology, 31, 1353–1378.
479 Brey, G.P., Doroshev, A.M., Girnis, A.V., and Turkin, A.I. (1999) Garnet–spinel–
480 olivine–orthopyroxene equilibria in the $FeO–MgO–Al_2O_3–SiO_2–Cr_2O_3$
481 system: I. Composition and molar volumes of minerals. European Journal of
482 Mineralogy, 11, 599–617.
483 Brueckner, H.K. (1998) Sinking intrusion model for the emplacement of
484 garnet-bearing peridotites into continent collision orogens. Geology, 26, 631–
485 634.
486 Brueckner, H.K., and Medaris, L.G. (2000) A general model for the intrusion and
487 evolution of ‘mantle’ garnet peridotites in high-pressure and
488 ultra-high-pressure metamorphic terranes. Journal of Metamorphic Geology,
489 18, 123–133.
490 Brueckner, H.K., Carswell, D.A., and Griffin, W.L. (2002) Paleozoic diamonds
491 within a Precambrian peridotite lens in UHP gneisses of the Norwegian
492 Caledonides. Earth and Planetary Science Letters, 203, 805–816.
493 Buob, A., Luth, R.W., Schmidt, M.W., and Ulmer, P. (2006) Experiments on $CaCO_3$–
494 $MgCO_3$ solid solutions at high pressure and temperature. American
495 Mineralogist, 91, 435–440.

Byrnes, A.P., and Wyllie, P.J. (1981) Subsolidus and melting relations for the join $CaCO_3$–$MgCO_3$ at 10 kbar. Geochimica et Cosmochimica Acta, 45, 321–328.

Carlson, W.D., and Rosenfeld, J.L. (1981) Optical determination of topotactic aragonite–calcite growth kinetics: metamorphic implications. The Journal of Geology, 89, 615–638.

Chen, S.Z., Yang, J.S., and Li, T.F. (2009) Petrological investigation of the Ganyu peridotite in the Sulu ultrahigh-pressure terrane, eastern China. Tectonophysics, 475, 383–395.

Chen, Y., Ye, K., Guo, S., Wu, T.F., and Liu, J.B. (2013a) Multistage metamorphism of garnet orthopyroxenites from the Maowu mafic–ultramafic complex, Dabieshan UHP terrane, eastern China. International Geology Review, 55, 1239–1260.

Chen, Y., Ye, K., Wu, Y.W., Guo, S., Su, B., and Liu, J.B. (2013b) Hydration and dehydration in the lower margin of a cold mantle wedge: implications for crust–mantle interactions and petrogeneses of arc magmas. International Geology Review, 55, 1506–1522.

Chen, Y., Su, B., and Guo, S. (2015) The Dabie–Sulu orogenic peridotites: progress and key issues. Science China Earth Sciences, 58, 1679–1699.

Chen, Y., Su, B., and Chu, Z.Y. (2017) Modification of an ancient subcontinental lithospheric mantle by continental subduction: Insight from the Maowu garnet peridotites in the Dabie UHP belt, eastern China. Lithos, 278–281, 54–71.

Dasgupta, R., Hirschmann, M.M., and Withers, A.C. (2004) Deep global cycling of carbon constrained by the solidus of anhydrous, carbonated eclogite under mantle conditions. Earth and Planetary Science Letters, 227, 73–85.

Dobrzhinetskaya, L., Green, H.W., and Wang, S. (1996) Alpe Arami: a peridotite massif from depths of more than 300 kilometers. Science, 271, 1841–1845.

Dobrzhinetskaya, L.F., Wirth, R., and Green, H.W. (2006) Nanometric inclusions of carbonates in Kokchetav diamonds from Kazakhstan: a new constraint for the depth of metamorphic diamond crystallization. Earth and Planetary Science Letters, 243, 85–93.

Droop, G.T.R. (1987) A general equation for estimating Fe^{3+} concentrations in ferromagnesian silicates and oxides from microprobe analyses, using stoichiometric criteria. Mineralogical magazine, 51, 431–435.

Fisler, D.K., and Cygan, R. (1999) Diffusion of Ca and Mg in calcite. American Mineralogist, 84, 1392–1399.

Franzolin, E., Merlini, M., Poli, S., and Schmidt, M.W. (2012) The temperature and compositional dependence of disordering in Fe-bearing dolomites. American Mineralogist, 97, 1676–1684.

Gebauer, D. (1996) A P–T–t path for an (ultra?-) high-pressure ultramafic/mafic rock-association and its felsic country-rocks based on SHRIMP-dating of magmatic and metamorphic zircon domains. Example: Alpe Arami (Central Swiss Alps). In A. Basu and S. Hart, Eds., Earth Processes: Reading the Isotopic Code, p. 307–329.

Gerya, T.V., Stöckhert, B., and Perchuk, A.L. (2002) Exhumation of high-pressure metamorphic rocks in a subduction channel: a numerical simulation. Tectonics, 21, doi:10.1029/2002TC001406.

Girnis, A.V., and Brey, G.P., Doroshev, A.M., Turkin, A.I., and Simon, N. (2003) The system $MgO–Al_2O_3–SiO_2–Cr_2O_3$ revisited: reanalysis of Doroshev et al.'s (1997) experiments and new experiments. European Journal of Mineralogy, 15, 953–964.

Grassi, D., and Schmidt, M.W. (2011) The melting of carbonated pelites from 70 to 700 km depth. Journal of Petrology, 52, 765–789.

Griffin, W.L., O'reilly, S.Y., Afonso, J.C., and Begg, G.C. (2009) The composition and evolution of lithospheric mantle: a re-evaluation and its tectonic implications. Journal of Petrology, 50, 1185–1204.

Guo, S., Ye, K., Cheng, N.F., Chen, Y., Su, B., and Liu, J.B. (2015) Metamorphic P–T trajectory and multi-stage fluid events of vein-bearing UHP eclogites from the Dabie terrane: insights from compositional zonations of key minerals. International Geology Review, 57, 1077–1102.

Hammouda, T. (2003) High-pressure melting of carbonated eclogite and experimental constraints on carbon recycling and storage in the mantle. Earth and Planetary Science Letters, 214, 357–368.

Harley, S.L. (1984) An experimental study of the partitioning of Fe and Mg between garnet and orthopyroxene. Contributions to Mineralogy and Petrology, 86, 359–373.

Hermann, J., Rubatto, D., and Trommsdorff, V. (2006) Sub-solidus Oligocene zircon formation in garnet peridotite during fast decompression and fluid infiltration (Duria, Central Alps). Mineralogy and Petrology, 88, 181–206.

Hermann, J., Troitzsch, U., and Scott, D. (2016) Experimental subsolidus phase relations in the system $CaCO_3–CaMg(CO_3)_2$ up to 6.5 GPa and implications for subducted marbles. Contributions to Mineralogy and Petrology, doi: 10.1007/s00410-016-1296-y.

Herzberg, C., Raterron, P., and Zhang, J. (2000) New experimental observations on the anhydrous solidus for peridotite KLB-1. Geochemistry, Geophysics, Geosystems, 1, Paper no. 2000GC000089.

Holland, T., and Powell, R. (2011) An improved and extended internally consistent thermodynamic dataset for phases of petrological interest, involving a new equation of state for solids. Journal of Metamorphic Geology, 29, 333–383.

Ionov, D.A., Dupuy, C., O'Reilly, S.Y., Kopylova, M.G., and Genshaft, Y.S. (1993) Carbonated peridotite xenoliths from Spitsbergen: implications for trace element signature of mantle carbonate metasomatism. Earth and Planetary Science Letters, 119, 283–297.

Irving, A., and Wyllie, P. (1975) Subsolidus and melting relationships for calcite, magnesite and the join $CaCO_3–MgCO_3$ 36 kb. Geochimica et Cosmochimica Acta, 39, 35–53.

Johannes, W., and Puhan, D. (1971) The calcite–aragonite transition, reinvestigated. Contributions to Mineralogy and Petrology, 31, 28–38.

John, T., and Schenk, V. (2003) Partial eclogitisation of gabbroic in a late Precambrian subduction zone (Zambia): prograde metamorphism triggered by fluid infiltration. Contributions to Mineralogy and Petrology, 146, 174–191.

Klemme, S. (2004) The influence of Cr on the garnet–spinel transition in the Earth's mantle: experiments in the system $MgO–Cr_2O_3–SiO_2$ and thermodynamic modelling. Lithos, 77, 639–646.

Kogarko, L.N., Kurat, G., and Ntaflos, T. (2001) Carbonate metasomatism the oceanic mantle beneath Fernando de Noronha island, Brazil. Contributions to Mineralogy and Petrology, 140, 577–587.

Korsakov, A.V., Gussem, K.D., Zhukov, V.P., Perraki, M., Vandenabeele, P., and Golovin, A.V. (2009) Aragonite–calcite–dolomite relationship in UHPM polycrystalline carbonate inclusions from the Kokchetav massif, northern Kazakhstan. European Journal of Mineralogy, 21, 1301–1311.

Kubo, K. (2002) Dunite formation processes in highly depleted peridotite: case study of the Iwanaidake peridotite, Hokkaido, Japan. Journal of Petrology, 43, 423–448.

Kushiro, I. (1975) Carbonate–silicate reactions at high pressures and possible presence of dolomite and magnesite in the upper mantle. Earth and Planetary Science Letters, 28, 116–120.

Lee, C.T.A. (2003) Compositional variation of density and seismic velocities in natural peridotites at STP conditions: implications for seismic imaging of compositional heterogeneities in the upper mantle. Journal of Geophysical Research: Solid Earth, 108, doi:10.1029/2003JB002413.

Leech, M.L. (2001) Arrested orogenic development: eclogitization, delamination, and tectonic collapse. Earth and Planetary Science Letters, 185, 149–159.

Li, H.Y., Chen, R.X., Zheng, Y.F., and Hu, Z.C. (2016) The crust–mantle interaction in continental subduction channel: zircon evidence from orogenic peridotite in the Sulu orogen. Journal of Geophysical Research: Solid Earth, 121, 687–712.

Li, S.G., Xiao, Y.L., Liou, D.L., Chen, Y.Z., Ge, N.J., Zhang, Z.Q., Sun, S.S., Cong, B.L., Zhang, R.Y., and Hart, S.R. (1993) Collision of the North China and Yangtse blocks and formation of coesite-bearing eclogites: timing and processes. Chemical Geology, 109, 89–111.

Liou, J.G., and Zhang, R.Y. (1996) Occurrences of intergranular coesite in ultrahigh-P rocks from the Sulu regions, eastern China: implications for lack of fluid during exhumation. American Mineralogist, 81, 1217–1221.

Liu, J.B., Ye, K., Maruyama, S., Cong, B.L., and Fan, H.R. (2001) Mineral inclusions in zircon from gneisses in the ultrahigh-pressure zone of the Dabie Mountains, China. The Journal of Geology, 109, 523–535.

Luth, R.W. (2001) Experimental determination of the reaction aragonite + magnesite = dolomite at 5 to 9 GPa. Contributions to Mineralogy and Petrology, 141, 222–232.

Lü, Z., Zhang, L.F., and Chen, Z.Y. (2014) Jadeite- and dolomite-bearing coesite

eclogite from western Tianshan, NW China. European Journal of Mineralogy, 26, 245–256.

Malaspina, N., Hermann, J., and Scambelluri, M. (2009) Fluid/mineral interaction in UHP garnet peridotite. Lithos, 107, 38–52.

Martinez, I., Zhang, J., and Reeder, R.J. (1996) In situ X-ray diffraction of aragonite and dolomite at high pressure and high temperature: evidence for dolomite breakdown to aragonite and magnesit. American Mineralogist, 81, 611–624.

Morishita, T., Arai, S., and Tamura, A. (2003) Petrology of an apatite-rich layer in the Finero phlogopite-peridotite, Italian western Alps; implications for evolution of metasomatising agent. Lithos, 69, 37–49.

Naemura, K., Hirajima, T., and Svojtka, M. (2009) The pressure–temperature path and the origin of phlogopite in spinel–garnet peridotites from the Blanský Les massif of the Moldanubian zone, Czech Republic. Journal of Petrology, 50, 1795–1827.

Nickel, K.G., and Green, D.H. (1985) Empirical geothermobarometry for garnet peridotites and implications for the nature of the lithosphere, kimberlites and diamonds. Earth and Planetary Science Letters, 73, 158–170.

O'Brien, P.J., and Ziemann, M.A. (2008) Preservation of coesite in exhumed eclogite: insights from Raman mapping. European Journal of Mineralogy, 20, 827–834.

Olker, B., Altherr, R., and Paquin, J. (2003) Fast exhumation of the ultrahigh-pressure Alpe Arami garnet peridotite (Central Alps, Switzerland): constraints from geospeedometry and thermal modelling. Journal of Metamorphic Geology, 21, 395–402.

Proyer, A., Rolfo, F., Zhu, Y.F., Castelli, D., and Compagnoni, R. (2013) Ultrahigh-pressure metamorphism in the magnesite + aragonite stability field: evidence from two impure marbles from the Dabie–Sulu UHPM belt. Journal of Metamorphic Geology, 31, 35–48.

Ravna, E.K. (2000) The garnet–clinopyroxene Fe^{2+}–Mg geothermometer: an updated calibration. Journal of Metamorphic Geology, 18, 211–219.

Ren, Y.F., Yang, J.S., Zhang, Z.M., and Li, T.F. (2007) Study of the Macaokuang peridotite body from the PP6 drill hole of the Chinese Continental Scientific Drilling (CCSD) project. Acta Geologica Sinica, 81, 1004–1016 (in Chinese with English abstract).

Sapienza, G.T., Scambelluri, M., and Braga, R. (2009) Dolomite-bearing orogenic garnet peridotites witness fluid-mediated carbon recycling in a mantle wedge (Ulten Zone, Eastern Alps, Italy). Contributions to Mineralogy and Petrology, 158, 401–420.

Sato, K., and Katsura, T. (2001) Experimental investigation on dolomite dissociation into aragonite + magnesite up to 8.5 GPa. Earth and Planetary Science Letters, 184, 529–534.

Scambelluri, M., Hermann, J., Morten, L., and Rampone, E. (2006) Melt-versus fluid-induced metasomatism in spinel to garnet wedge peridotites (Ulten Zone, Eastern Italian Alps): clues from trace element and Li abundances.

672 Contributions to Mineralogy and Petrology, 151, 372–394.
673 Scambelluri, M., Pettke, T., and Van Roermund, H. (2008) Majoritic garnets monitor
674 deep subduction fluid flow and mantle dynamics. Geology, 36, 59–62.
675 Scambelluri, M., Pettke, T., Rampone, E., Godard, M., and Reusser, E. (2014)
676 Petrology and trace element budgets of high-pressure peridotites indicate
677 subduction dehydration of serpentinized mantle (Cima di Gagnone, Central
678 Alps, Switzerland). Journal of Petrology, 55, 459–498.
679 Schertl, H.P., Schreyer, W., and Chopin, C. (1991) The pyrope–coesite rocks and
680 their country rocks at Parigi, Dora Maira massif, western Alps: detailed
681 petrography, mineral chemistry and PT-path. Contributions to Mineralogy
682 and Petrology, 108, 1–21.
683 Shirasaka, M., Takahashi, E., Nishihara, Y., Matsukage, K., and Kikegawa, T. (2002)
684 In situ X-ray observation of the reaction dolomite = aragonite + magnesite at
685 900–1300 K. American Mineralogist, 87, 922–930.
686 Song, S.G., Zhang, L.F., and Niu, Y.L. (2004) Ultra-deep origin of garnet peridotite
687 from the North Qaidam ultrahigh-pressure belt, Northern Tibetan Plateau,
688 NW China. American Mineralogist, 89, 1330–1336.
689 Song, S.G., Su, L., Niu, Y.L., Lai, Y., and Zhang, L.F. (2009) CH_4 inclusions in
690 orogenic harzburgite: evidence for reduced slab fluids and implication for
691 redox melting in mantle wedge. Geochimica et Cosmochimica Acta, 73,
692 1737–1754.
693 Spengler, D., Van Roermund, H.L., Drury, M.R., Ottolini, L., Mason, P.R., and
694 Davies, G.R. (2006) Deep origin and hot melting of an Archaean orogenic
695 peridotite massif in Norway. Nature, 440, 913–917.
696 Su, B., Chen, Y., Guo, S., Chu, Z.Y., Liu, J.B., and Gao, Y.J. (2016a) Carbonatitic
697 metasomatism in orogenic dunites from Lijiatun in the Sulu UHP terrane,
698 eastern China. Lithos, 262, 266–284.
699 Su, B., Chen, Y., Guo, S., and Liu, J.B. (2016b) Origins of orogenic dunites:
700 petrology, geochemistry, and implications. Gondwana Research, 29, 41–59.
701 Thomsen, T.B., and Schmidt, M.W. (2008) Melting of carbonated pelites at 2.5–5.0
702 Gpa, silicate–carbonate liquid immiscibility, and potassium–carbon
703 metasomatism of the mantle. Earth and Planetary Science Letters, 267, 17–
704 31.
705 van Roermund, H.L.M., and Drury, M.R. (1998) Ultra-high pressure (P>6 GPa)
706 garnet peridotites in Western Norway: exhumation of mantle rocks
707 from >185 km depth. Terra Nova, 10, 295–301.
708 van Roermund, H.L.M., Carswell, D.A., Drury, M.R., Heijboer, T.C. (2002)
709 Microdiamonds in a megacrystic garnet websterite pod from Bardane on the
710 island of Fjørtoft, western Norway: evidence for diamond formation in
711 mantle rocks during deep continental subduction. Geology, 30, 959–962.
712 Walter, M.J. (1998) Melting of garnet peridotite and the origin of komatiite and
713 depleted lithosphere. Journal of Petrology, 39, 29–60.
714 Whitney, D.L., and Evans, B.W. (2010) Abbreviations for names of rock-forming
715 minerals. American mineralogist, 95, 185–187.

Wyllie, P.J, Huang, W.L., Otto, J., and Byrnes, A. (1983) Carbonation of peridotites and decarbonation of siliceous dolomites represented in the system CaO–MgO–SiO_2–CO_2 to 30 kbar. Tectonophysics, 100, 359–388.

Xie, Z.P., Hattori, K., and Wang, J. (2013) Origins of ultramafic rocks in the Sulu ultrahigh-pressure terrane, Eastern China. Lithos, 178, 158–170.

Xu, S.T., Okay, A.I., Ji, S.Y., Sengor, A.M.C., Su, W., Liu, Y.C., and Jiang, L.L. (1992) Diamond from the Dabie shan metamorphic rocks and its implication for tectonic setting. Science, 256, 80–82.

Yamato, P., and Brun, J.P. (2017) Metamorphic record of catastrophic pressure drops in subduction zones. Nature Geoscience, 10, 46–50.

Yang, J.J., and Jahn, B.M. (2000) Deep subduction of mantle-derived garnet peridotites from the Su–Lu UHP metamorphic terrane in China. Journal of Metamorphic Geology, 18, 167–180.

Ye, K., Cong, B.L., and Ye, D.N. (2000a) The possible subduction of continental material to depths greater than 200 km. Nature, 407, 734–736.

Ye, K., Yao, Y.P., Katayama, I., Cong, B.L., Wang, Q.C., and Maruyama, S. (2000b) Large areal extent of ultrahigh-pressure metamorphism in the Sulu ultrahigh-pressure terrane of East China: new implications from coesite and omphacite inclusions in zircon of granitic gneiss. Lithos, 52, 157–164.

Ye, K., Song, Y.R., Chen, Y., Xu, H.J., Liu, J.B., and Sun, M. (2009) Multistage metamorphism of orogenic garnet-lherzolite from Zhimafang, Sulu UHP terrane, E. China: implications for mantle wedge convection during progressive oceanic and continental subduction. Lithos, 109, 155–175.

Zanetti, A., Mazzucchelli, M., Rivalenti, G., and Vannucci, R. (1999) The Finero phlogopite-peridotite massif: an example of subduction-related metasomatism. Contributions to Mineralogy and Petrology, 134, 107–122.

Zhang, J.Z., Li, B.S., Utsumi, W., and Liebermann, R.C. (1996) In situ X-ray observations of the coesite–stishovite transition: reversed phase boundary and kinetics. Physics and Chemistry of Minerals, 23(1), 1–10.

Zhang, L.F., Ellis, D.J., Arculus, R.J., Jiang, W., and Wei, C.J. (2003) 'Forbidden zone' subduction of sediments to 150 km depth—the reaction of dolomite to magnesite + aragonite in the UHPM metapelites from western Tianshan, China. Journal of metamorphic Geology, 21, 523–529.

Zhang, R.Y., and Liou, J.G. (1996) Coesite inclusions in dolomite from eclogite in the southern Dabie Mountains, China: the significance of carbonate minerals in UHPM rocks. American Mineralogist, 81, 181–186.

Zhang, R.Y., Liou, J.G., Yang, J.S., and Yui, T.F. (2000) Petrochemical constraints for dual origin of garnet peridotites from the Dabie–Sulu UHP terrane, eastern–central China. Journal of Metamorphic Geology, 18, 149–166.

Zhang, R.Y., Li, T., Rumble, D., Yui, T.F., Li, L., Yang, J.S., Pan, Y.M., and Liou, J.G. (2007) Multiple metasomatism in Sulu ultrahigh-P garnet peridotite constrained by petrological and geochemical investigations. Journal of Metamorphic Geology, 25, 149–164.

Zhang, R.Y., Pan, Y.M., Yang, Y.H., Li, T.F., Liou, J.G., and Yang, J.S. (2008)

760 Chemical composition and ultrahigh-P metamorphism of garnet peridotites
761 from the Sulu UHP terrane, China: investigation of major, trace elements and
762 Hf isotopes of minerals. Chemical Geology, 255, 250–264.
763 Zhang, R.Y., Liou, J.G., and Ernst, W.G. (2009) The Dabie–Sulu continental
764 collision zone: A comprehensive review. Gondwana Research, 16, 1–26.
765 Zheng, J.P., Sun, M., Griffin, W.L., Zhou, M.F., Zhao, G.C., Robinson, R., Tang,
766 H.Y., and Zhang, Z.H. (2008) Age and geochemistry of contrasting peridotite
767 types in the Dabie UHP belt, eastern China: petrogenetic and geodynamic
768 implications. Chemical Geology, 247, 282–304.
769 Ziberna, L., Klemme, S., and Nimis, P. (2013) Garnet and spinel in fertile and
770 depleted mantle: insights from thermodynamic modelling. Contributions to
771 Mineralogy and Petrology, 166, 411–421.

FIGURE CAPTIONS

FIGURE 1. Geological sketch map of the Sulu ultra-high pressure metamorphic terrane in eastern China (modified from Ye et al. 2000b). Abbreviations: YQW, Yantai–Qingdao–Wulian; JX, Jiashan–Xiangshui.

FIGURE 2. (**a**) Field photograph of the Lijiatun dunite block. (**b**) BSE image of a calcite veinlet along the grain boundaries of matrix olivines. (**c**) Photomicrograph in plane-polarized light showing isolated carbonates as intergranular grains in the orthopyroxene-absent domain. (**d–f**) Photomicrographs of representative carbonate grains with low dihedral angles against surrounding olivines in plane-polarized light. (**g–i**) BSE images showing symplectite-like magnesite and calcite intergrowths in matrix; the bright and dark areas correspond to calcite and magnesite, respectively.

FIGURE 3. Representative BSE images and X-ray intensity maps of carbonate phases in the Lijiatun dunites. (**a–b**) BSE images showing the microtexture and mineral modal percentages of magnesite and calcite in the carbonate intergrowths. The inset shows the Raman spectrum of calcite. (**c–d**) Dolomite relicts after their breakdown into magnesite and aragonite (transformed to calcite at low pressure). Dolomite Raman spectrum is given in the inset. (**e–f**) X-ray intensity maps of the carbonate intergrowths with dolomite relict inclusions, corresponding to the BSE image of (**d**).

FIGURE 4. (**a**) BSE images showing the interstitial garnets with small grain sizes in the matrix olivine domain. (**b–d**) Detailed views of garnet grains without any retrograde rims. (**c**) The black line with an arrow shows the position of the profile for EPMA analysis of garnet major elements presented in Fig. 5(b). (**e**) BSE image of coexisting chlorite and amphibole after an orthopyroxene porphyroblast. (**f**) Photomicrograph taken with cross-polarized light showing anhedral talc and amphibole in matrix. (**g**) Photograph of an amphibole vein approximately one centimeter wide in the dunite block.

FIGURE 5. Compositional profile of pyrope (Prp), almandine (Alm), grossular (Grs), knorringite (Knor) and andradite (Adr) in the representative garnet along the A–A' in Figure 4(c).

FIGURE 6. FIB cross-sectioning of the carbonate intergrowth and transmission electron microscope (TEM) results. (**a**) BSE image of the sampled area prior to the cross-sectioning. The dotted rectangle shows the position where the platinum layer is deposited; (**b**) Secondary electron image of the FIB-cut section after ion polish; (**c**) Bright field TEM image of the calcite and magnesite intergrowth. The inset shows the high-resolution TEM image across the interface between calcite and magnesite. The five yellow circles represent the analysis positions of TEM-EDS; (**d–h**) TEM-EDS spectra of carbonate phases corresponding to the five points shown in the inset of (**c**),

816 respectively. The inset of (**d**) shows selected-area electron diffraction (SAED) pattern
817 for calcite.
818
819 **FIGURE 7.** Integrated *P–T* path for the whole geodynamic history of the Lijiatun
820 dunites. As stated by Su et al. (2016a) and this study, (1) these dunites originated from
821 the SCLM beneath the NCC and suffered high-degree melting in the early Proterozoic.
822 (2) They were metasomatized by dolomitic melt with formation of Ol-rich,
823 Cpx-bearing veins crosscutting Opx in the shallow SCLM. Some Dol grains
824 crystallized from such a melt infiltration in Opx-absent domains. (3) In the Triassic,
825 these dunites were incorporated into the subduction channel and experienced
826 ultra-deep subduction. Trace Grt was produced in matrix. (4) At the peak stage (P~5
827 GPa), Dol broke down into Mgs and Arg. (5) Arg was replaced by Cal during
828 exhumation to shallow depths. (6) At last, the dunites were infiltrated by slab-derived
829 fluids and pyroxenes were partially replaced by Amp and minor Tlc and Chl.
830 Abbreviations: JP71 = Johannes and Puhan (1971); KU75 = Kushiro et al. (1975);
831 MA96 = Martinez et al. (1996); HZ00 = Herzberg et al. (2000); LU01 = Luth (2001);
832 SK01 = Sato and Katsura (2001); SH02 = Shirasaka et al. (2002); BU06 = Buob et al.
833 (2006); JH16=Hermann et al. (2016).

This is a preprint, the final version is subject to change, of the American Mineralogist (MSA)
Cite as Authors (Year) Title. American Mineralogist, in press.
(DOI will not work until issue is live.) DOI: http://dx.doi.org/10.2138/am-2017-5982

TABLE 1. Representative major element compositions of carbonate minerals.

Mineral	Cal (after Arg)						Mgs				Cal-Mgs intergrowth
An. no.	23	24	29	30	31	52	37	38	62	63	broad beam (Ave. n=12)
SiO_2	0.09	0.09	0.09	0.08	0.10	0.02	0.36	0.14	0.28	0.38	0.19
FeO	0.20	0.18	0.22	0.16	0.20	0.24	8.48	8.86	6.79	7.14	3.47
MnO	0.08	0.02	0.01	0.07	0.04	0.03	0.53	0.36	0.37	0.38	0.12
MgO	0.11	0.11	0.48	0.90	0.50	0.13	42.81	42.54	43.52	42.60	20.93
CaO	55.25	55.92	53.16	53.08	57.75	55.44	0.11	0.09	0.03	0.05	30.62
SrO	bdl	bdl	bdl	bdl	bdl	bdl	bdl	0.02	0.01	0.03	bdl
BaO	bdl	0.03	bdl	0.01	0.01	0.01	0.02	bdl	bdl	bdl	0.01
Total	55.72	56.35	53.96	54.29	58.59	55.86	52.31	52.01	51.00	50.58	55.33
CO_2 (100-tot.)	44.28	43.65	46.04	45.71	41.41	44.14	47.69	47.99	49.01	49.42	44.67
Fe	0.003	0.002	0.003	0.002	0.003	0.003	0.099	0.104	0.080	0.085	0.043
Mn	0.001	0.000	0.000	0.001	0.001	0.000	0.006	0.004	0.004	0.005	0.001
Mg	0.003	0.003	0.012	0.023	0.012	0.003	0.893	0.890	0.915	0.909	0.466
Ca	0.993	0.995	0.984	0.974	0.985	0.993	0.002	0.001	0.000	0.001	0.490
Σ cations	1.0	1.0	1.0	1.0	1.0	1.0	1.0	1.0	1.0	1.0	1.0
CO_3^{2-}	1.015	0.989	1.086	1.069	0.900	1.008	0.911	0.920	0.944	0.966	0.910
$Ca/(Ca+Mg+Fe^{2+}+Mn)$	0.99	0.99	0.98	0.97	0.99	0.99	0.00	0.00	0.00	0.00	0.49
$Mg/(Mg+Fe^{2+})$	0.49	0.51	0.79	0.91	0.82	0.48	0.90	0.90	0.92	0.91	0.92

Notes: Cal–Mgs intergrowth was analyzed using a broad beam (d=20 μm); bdl, Below detection limit.

This is a preprint, the final version is subject to change, of the American Mineralogist (MSA)
Cite as Authors (Year) Title. American Mineralogist, in press.
(DOI will not work until issue is live.) DOI: http://dx.doi.org/10.2138/am-2017-5982

TABLE 2. Representative major element compositions of garnet, orthopyroxene, clinopyroxene and amphibole.

Mineral	Grt						Opx		Cpx		Amp	
Texture	core	core	core	rim	rim	rim	core	rim	-	-	-	-
An. no.	349	347	133	21	106	60	442	135	32	151	25	473
SiO_2	41.38	41.37	41.84	42.14	41.41	41.43	56.40	58.02	55.00	55.04	46.32	46.87
TiO_2	bdl	bdl	0.02	0.02	0.03	0.03	0.03	0.01	bdl	0.01	0.39	0.42
Al_2O_3	22.21	22.36	22.31	21.98	23.48	22.66	1.93	0.45	0.68	0.74	12.08	11.90
Cr_2O_3	1.12	1.13	1.22	1.19	0.95	1.06	0.95	0.05	0.25	0.64	1.32	1.50
FeO	9.18	9.26	9.38	9.76	9.91	10.56	5.18	5.43	1.16	1.23	3.02	2.84
MnO	0.75	0.78	0.75	0.69	0.83	0.71	0.12	0.13	0.03	0.05	0.05	0.03
MgO	18.93	19.04	19.53	19.70	19.31	19.29	33.82	36.06	18.07	17.90	18.82	18.60
CaO	4.93	4.69	4.40	4.28	4.14	4.43	1.49	0.10	23.82	23.22	12.33	12.37
Na_2O	0.01	0.04	0.01	bdl	0.01	0.00	0.04	bdl	0.29	0.63	1.74	1.77
K_2O	0.01	0.01	0.01	0.01	0.01	0.01	0.01	0.01	bdl	bdl	0.60	0.43
NiO	0.04	bdl	0.04	bdl	0.02	0.03	0.07	0.06	0.02	bdl	0.10	0.11
Total	98.55	98.68	99.52	99.76	100.09	100.20	100.05	100.34	99.31	99.46	96.77	96.84
Si	3.002	2.997	3.004	3.018	2.956	2.961	1.944	1.981	2.000	1.996	6.535	6.603
Ti	0	0	0.001	0.001	0.001	0.001	0.001	0	0	0	0.041	0.045
Al	1.900	1.909	1.888	1.855	1.975	1.909	0.078	0.018	0.029	0.032	2.009	1.977
Cr	0.064	0.065	0.069	0.067	0.054	0.060	0.026	0.001	0.007	0.018	0.147	0.167
Fe^{3+}	0.024	0.027	0.026	0.038	0.051	0.102	0.009	0.019	0	0.001	0.193	0.167
Fe^{2+}	0.533	0.535	0.537	0.546	0.540	0.529	0.141	0.136	0.035	0.036	0.164	0.168
Mn	0.046	0.048	0.046	0.042	0.050	0.043	0.004	0.004	0.001	0.001	0.006	0.004

Mg	2.048	2.056	2.091	2.104	2.055	2.055	1.738	1.835	0.979	0.967	3.957	3.905
Ca	0.383	0.364	0.339	0.328	0.317	0.339	0.055	0.004	0.928	0.903	1.864	1.867
Na	0.002	0.005	0.002	0	0.001	0	0.003	0	0.021	0.045	0.476	0.483
K	0.001	0.001	0.001	0.001	0.001	0.001	0	0.001	0	0	0.107	0.077
Ni	0.002	0	0.002	0	0.001	0.002	0.002	0.002	0.001	0	0.011	0.013
Cation	8.0	8.0	8.0	8.0	8.0	8.0	4.0	4.0	4.0	4.0	15.5	15.5
Mg#	79.36	79.36	79.57	79.38	79.19	79.52	92.50	93.10	96.54	96.42	96.02	95.87
mol%												
Alm	18.0	18.1	18.1	18.4	18.6	18.1						
Prp	65.9	66.3	67.0	67.2	68.0	67.5						
Grs	11.7	11.0	10.1	9.1	8.3	6.6						
Adr	1.2	1.3	1.3	1.9	2.5	4.9						
Knor	3.2	3.2	3.5	3.4	2.6	2.9						

Notes: bdl, Below detection limit. Knor = knorringite $Cr/(Cr+Al+Fe^{3+})$, Adr = andradite $Fe^{3+}/(Cr+Al+Fe^{3+})$, Alm = almandine $Fe^{2+}/(Fe^{2+}+Mg–Knor\times3+Ca–Adr\times3)\times Al/(Cr+Al+Fe^{3+})$, Prp = pyrope $(Mg–Knor\times3)/(Fe^{2+}+Mg–Knor\times3+Ca–Adr\times3)\times Al/(Cr+Al+Fe^{3+})$, Grs = grossular $(Ca–Adr\times3)/(Fe^{2+}+Mg–Knor\times3+Ca–Adr\times3)\times Al/(Cr+Al+Fe^{3+})$.

This is a preprint, the final version is subject to change, of the American Mineralogist (MSA)
Cite as Authors (Year) Title. American Mineralogist, in press.
(DOI will not work until issue is live.) DOI: http://dx.doi.org/10.2138/am-2017-5982

Figure 1

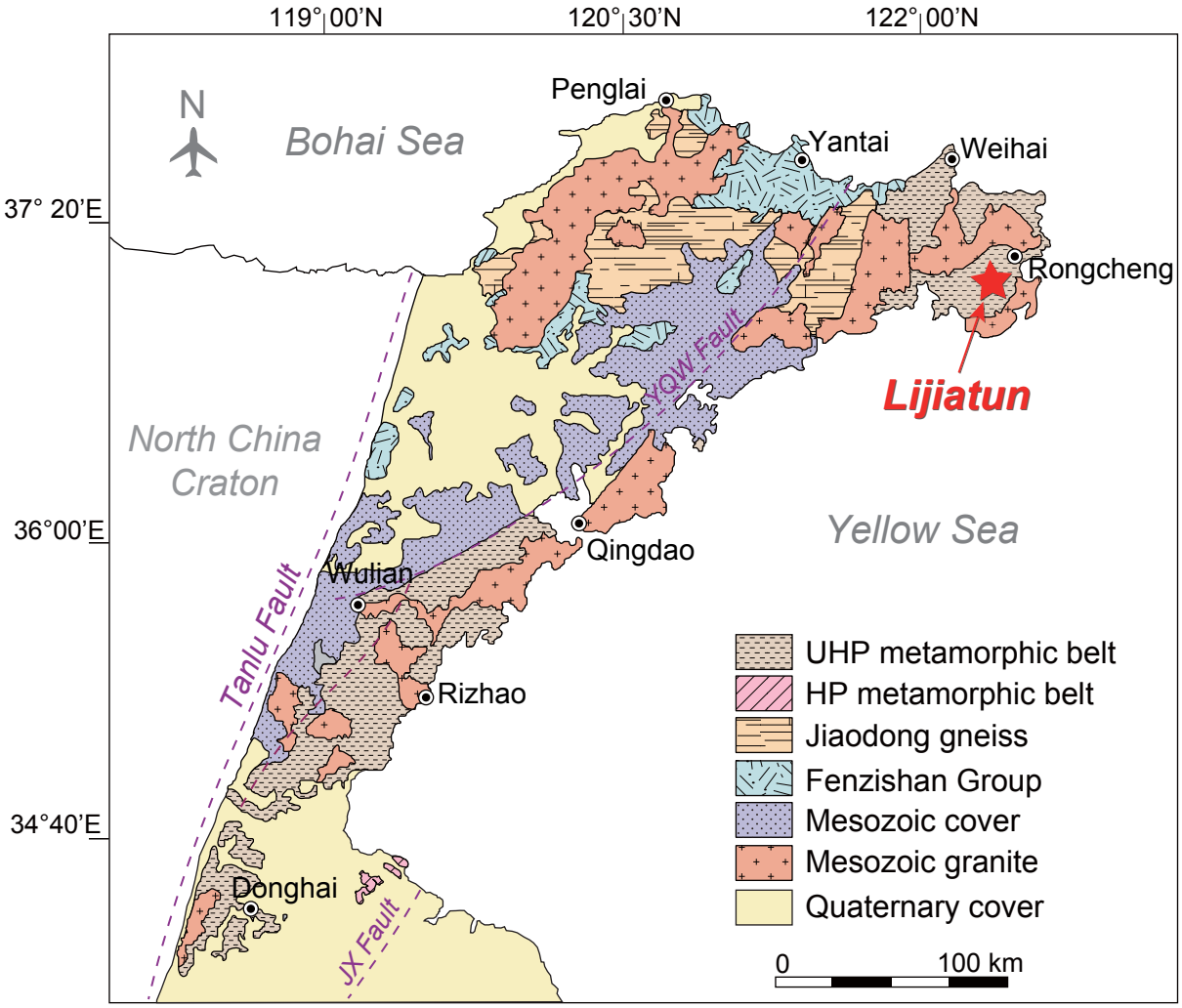

This is a preprint, the final version is subject to change, of the American Mineralogist (MSA)
Cite as Authors (Year) Title. American Mineralogist, in press.
(DOI will not work until issue is live.) DOI: http://dx.doi.org/10.2138/am-2017-5982

Figure 2

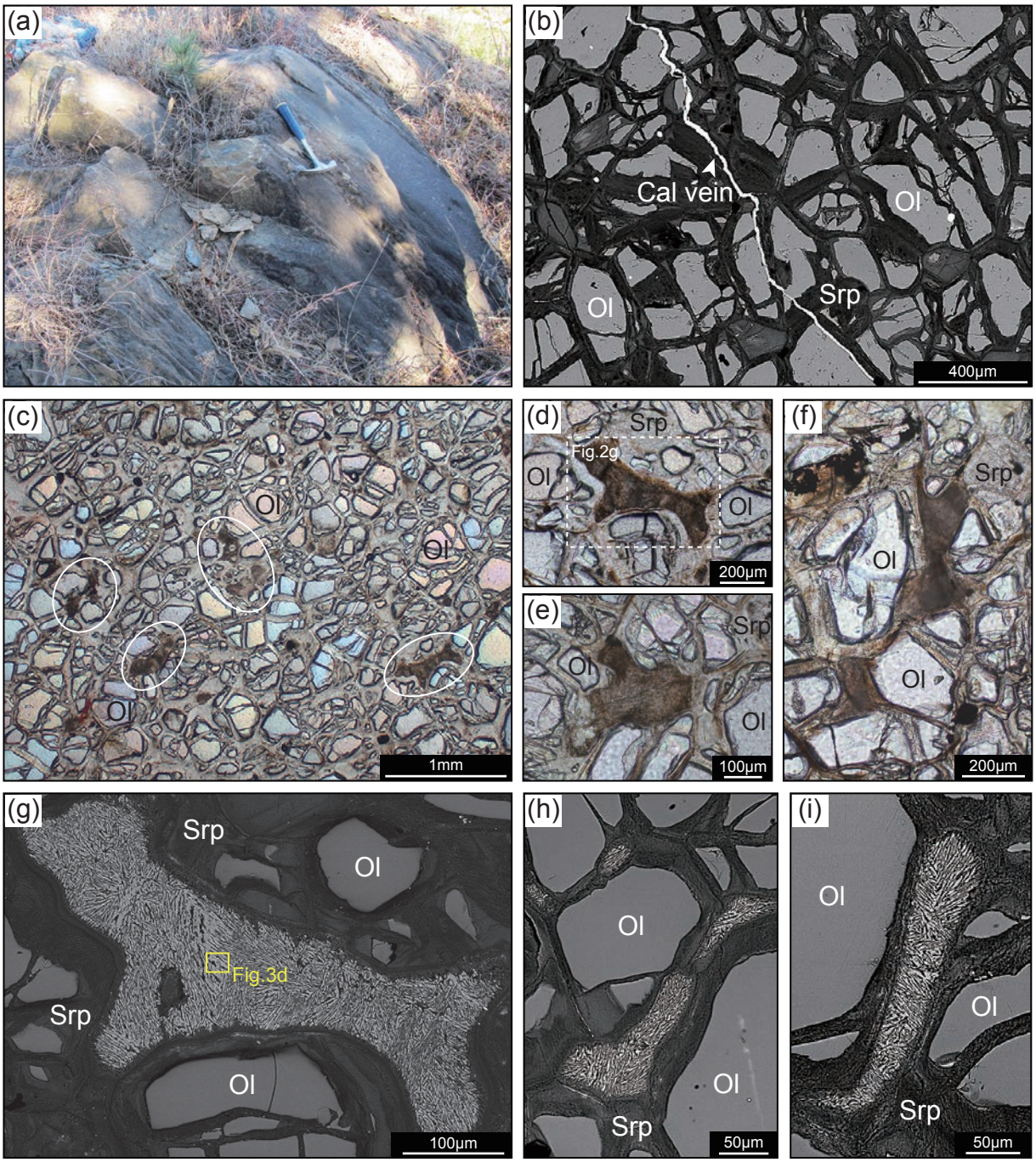

This is a preprint, the final version is subject to change, of the American Mineralogist (MSA)
Cite as Authors (Year) Title. American Mineralogist, in press.
(DOI will not work until issue is live.) DOI: http://dx.doi.org/10.2138/am-2017-5982

Figure 3

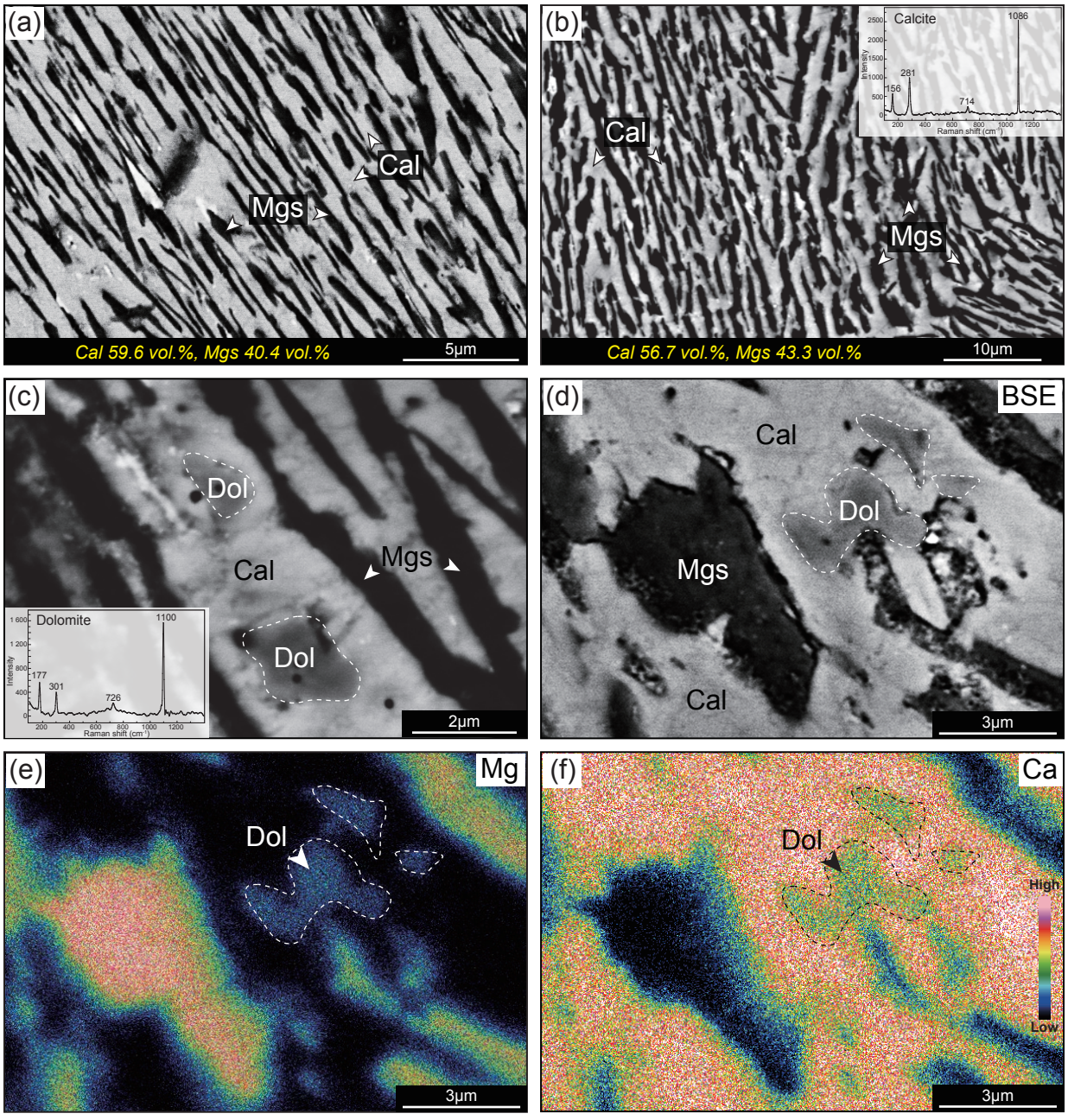

This is a preprint, the final version is subject to change, of the American Mineralogist (MSA)
Cite as Authors (Year) Title. American Mineralogist, in press.
(DOI will not work until issue is live.) DOI: http://dx.doi.org/10.2138/am-2017-5982

Figure 4

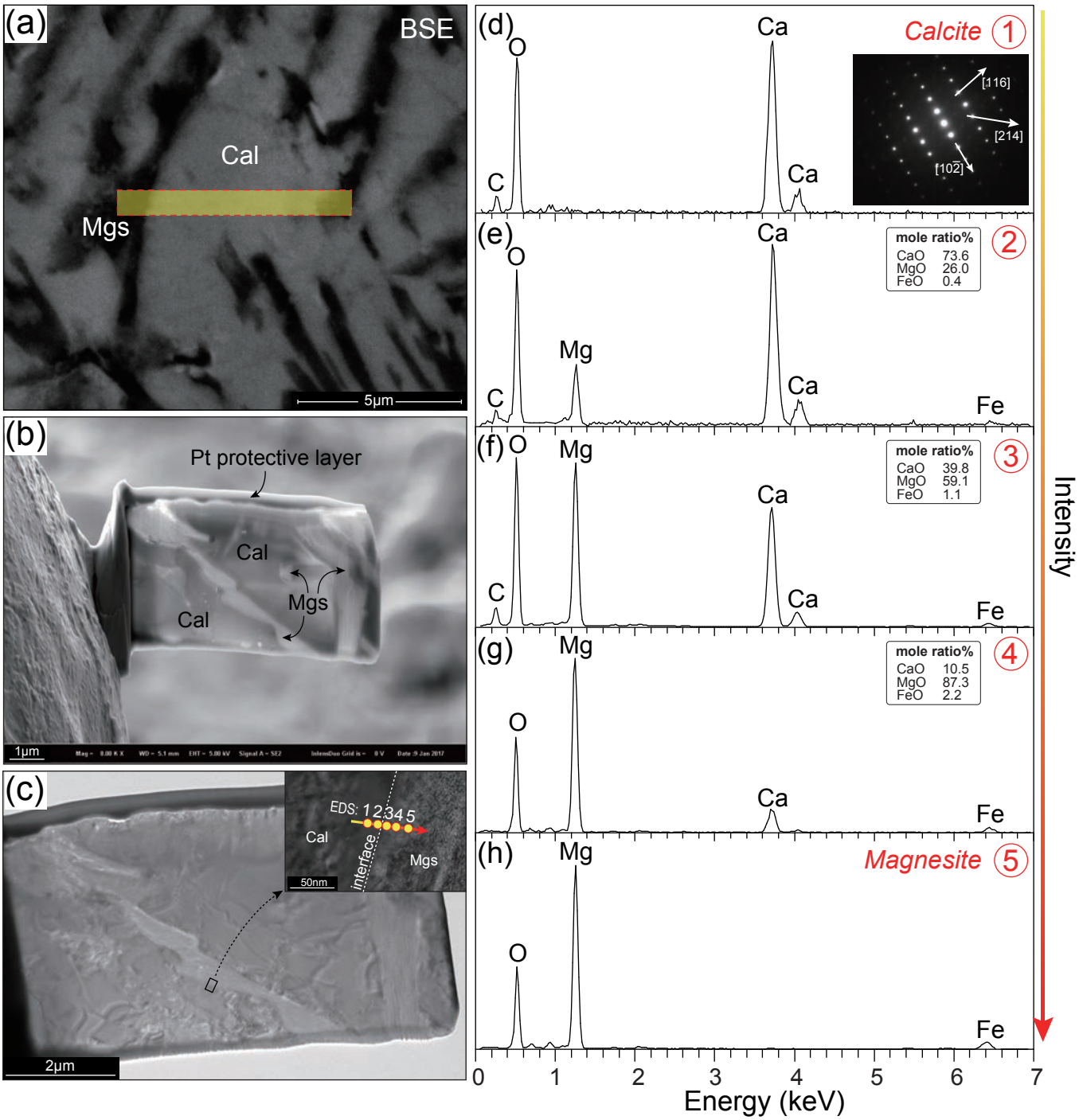

This is a preprint, the final version is subject to change, of the American Mineralogist (MSA)
Cite as Authors (Year) Title. American Mineralogist, in press.
(DOI will not work until issue is live.) DOI: http://dx.doi.org/10.2138/am-2017-5982

Figure 5

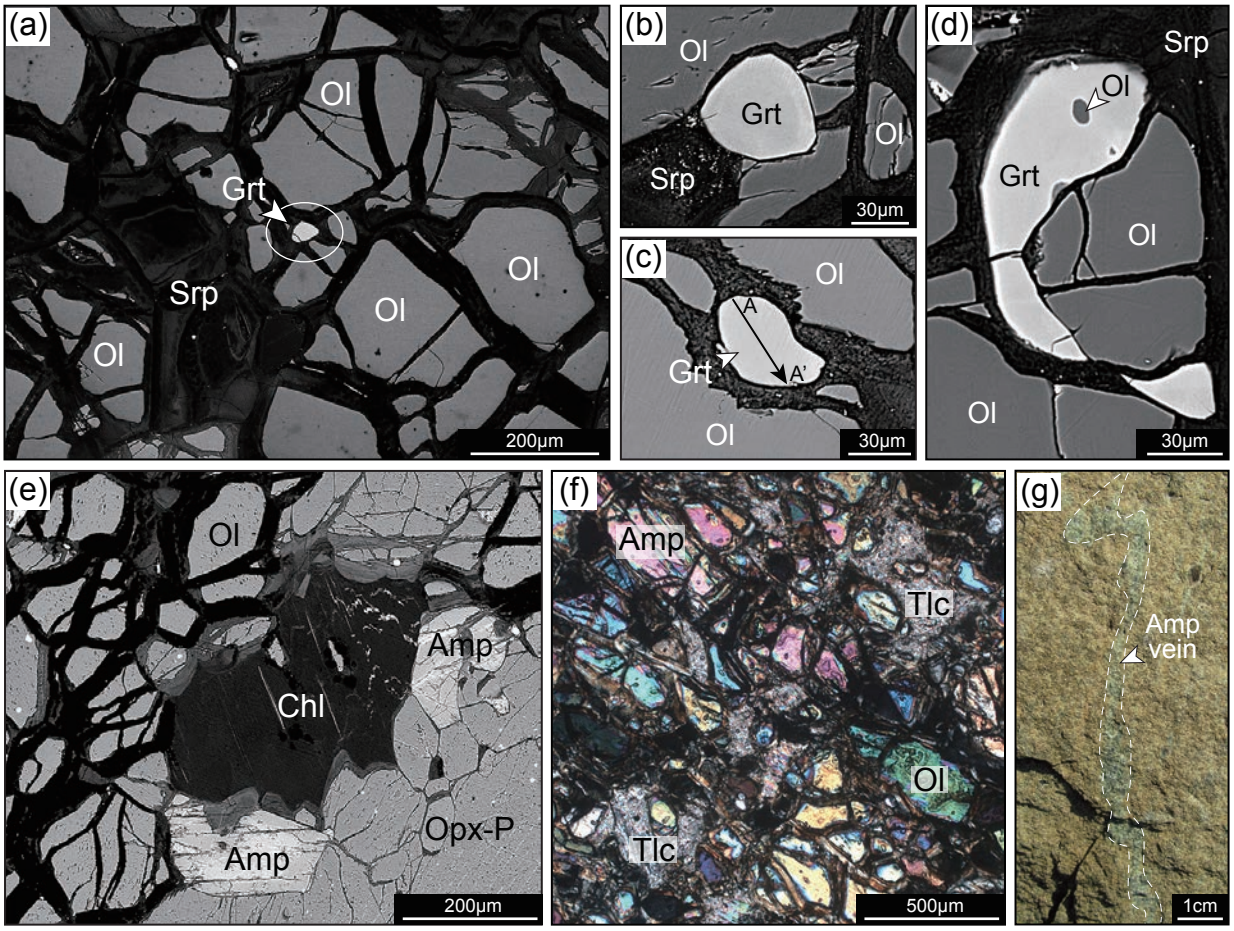

This is a preprint, the final version is subject to change, of the American Mineralogist (MSA)
Cite as Authors (Year) Title. American Mineralogist, in press.
(DOI will not work until issue is live.) DOI: http://dx.doi.org/10.2138/am-2017-5982

Figure 6

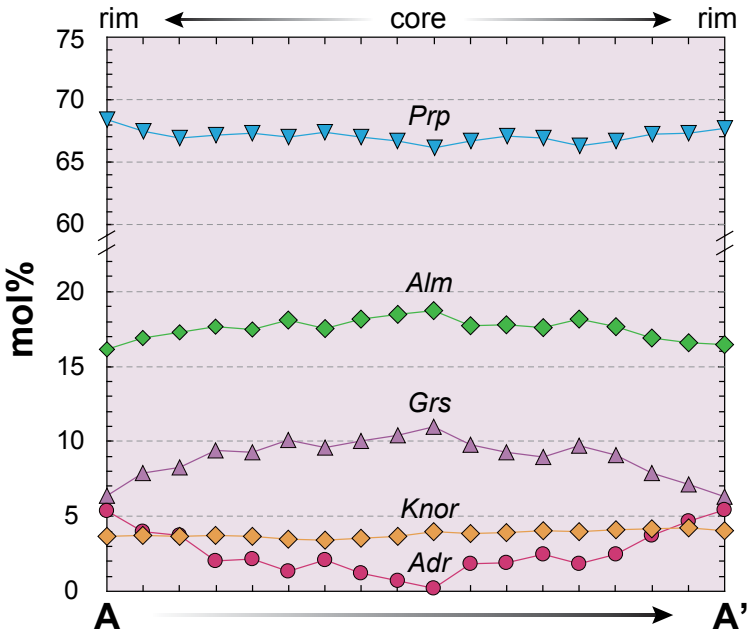

This is a preprint, the final version is subject to change, of the American Mineralogist (MSA)
Cite as Authors (Year) Title. American Mineralogist, in press.
(DOI will not work until issue is live.) DOI: http://dx.doi.org/10.2138/am-2017-5982

Figure 7